ARTICLE OPEN

Check for updates

Hexavalent chromium reduction and Rhodamine B degradation by visible-light-driven photocatalyst of stannum indium sulfide-samarium vanadate

Shahrzad Asoubar[1], Ali Mehrizad [iD][2 ✉], Mohammad A. Behnajady [iD][2], Mohammad Ebrahim Ramazani[1,3] and Parvin Gharbani [iD][4,5]

In this study, a flower-like $SnIn_4S_8/SmVO_4$ heterostructure was synthesized by applying a hydrothermal approach and used as a visible-light-driven photocatalyst to remove hexavalent chromium (Cr^{6+}) and Rhodamine B (RhB). The process design and optimization were carried out by response surface methodology (RSM). An artificial neural network (ANN) was also used to determine the relative importance of operational factors. Under RSM-based optimal conditions, the Cr^{6+} and RhB removal efficiency reached 90.93 and 97.57%, respectively. Process modeling by ANN revealed pH as the most influential factor in Cr^{6+} and dye removal. The predominant photocatalytic activity of $SnIn_4S_8/SmVO_4$ was attributed to its Z-scheme structure, leading to the significant separation of charge carriers and conserving the redox capacity of the photogenerated electron-holes. Kinetic studies revealed that the $SnIn_4S_8/SmVO_4$ could achieve considerable rate constants of 0.036 and 0.080 min^{-1} to remove Cr^{6+} and RhB, respectively. Furthermore, the catalyst's reusability was confirmed under optimal conditions.

INTRODUCTION

Contamination of aquatic environments by organic and inorganic pollutants has always been a concern from an environmental perspective. Dyes and heavy metals are among the main organic and inorganic compounds existing in most industries' wastewater. Rhodamine B (RhB) and hexavalent chromium (Cr(VI) or Cr^{+6}), selected as the organic dye and heavy metal ion models in this research, are among the water pollutants whose harms have been widely reported. RhB is a synthetic and fluorescein dye commonly used in textile and dyeing with proven carcinogenic and teratogenic effects on public health. In 2019, Cr^{6+} compounds were introduced among the first category of hypertoxic water contaminants. When released directly into the water, such chemicals will cause irreparable damage to flora and fauna life by disrupting photosynthetic processes and cytotoxicity. In addition, they lead to various diseases, such as ulcers, respiratory problems, kidney and liver damage, and lung cancer in humans[1–9]. Therefore, urgent action is necessary to prevent them from entering aquatic environments.

Accordingly, tremendous efforts have been devoted to addressing water pollutants. However, advanced oxidation processes (AOPs) seem to have aroused plentiful interest due to their unique features in converting pollutants into harmless compounds[10–14]. Photocatalysis mediated by semiconductors is one of the AOPs capable of forming a reduction/oxidation (redox) process to efficiently reduce heavy metals and organic dyes without secondary pollution efficiently[15–18]. Regarding energy crisis issues, exploiting responsive semiconductors for cost-effective irradiation sources like visible/solar light is indispensable. Stannum indium sulfide ($SnIn_4S_8$) is a ternary chalcogenide semiconductor with potential uses in photocatalysis regarding its relatively narrow band gap, high stability, and strong visible-light absorption capacity. Generally, the short lifetime of photoinduced electron-hole (e^-h^+) pairs dramatically restricts the performance of the simplex catalyst, where $SnIn_4S_8$ is no

exception[19,20]. Among the extensive efforts to overcome this dilemma and improve efficiency, constructing $SnIn_4S_8$-based heterostructures enhance its performance[21–25]. In this respect, photocatalysts with Z-scheme heterostructure have a privileged position because of separating charge carriers and conserving the redox capacity of the photogenerated e^-h^+ pairs[26–28]. Researchers have reported various $SnIn_4S_8$-based Z-scheme photocatalysts. For instance, Shi et al. prepared Z-scheme flower-like $Bi_2S_3/SnIn_4S_8$ heterostructure and reported its higher performance than pure $SnIn_4S_8$ and Bi_2S_3 in photocatalytic degradation of RhB[29]. Zhang et al. successfully synthesized the Z-scheme heterojunction of $SnIn_4S_8$-CdS with enhanced photocatalytic redox capabilities[30]. Shen et al. showed that Z-scheme $SnIn_4S_8/CeO_2$ heterojunction could be used in the photocatalytic reduction of Cr^{6+} under visible light[31]. Tang et al. reported the g-$C_3N_4/SnIn_4S_8$ composite as a direct Z-scheme photocatalyst to enhance photoactivity and stability in eliminating dyes and heavy metals[32]. Despite the tremendous advances in this field, choosing an efficient semiconductor with suitable band edges is still essential for fabricating more $SnIn_4S_8$-based Z-scheme heterostructures with high photocatalytic efficiency and practical applications. Recently, rare-earth elements and their compounds have been considered in photocatalytic studies regarding their unique electronic and optical features[33]. In this respect, samarium vanadate ($SmVO_4$) can be considered a promising semiconductor candidate owning to its relatively narrow band gap, visible-light harvesting capability, and suitable band structure for photoredox reactions[34]. The capability of $SmVO_4$ to form heterojunctions with other semiconductors has been investigated in various studies[35–40].

Considering the energy band alignment with $SnIn_4S_8$, $SmVO_4$ is expected as a good alternative for fabricating a Z-scheme heterojunction with high photocatalytic activity. However, to our knowledge, no related study has yet been conducted on $SnIn_4S_8/SmVO_4$ heterojunction.

[1]Department of Environmental Engineering, Tabriz Branch, Islamic Azad University, Tabriz, Iran. [2]Department of Chemistry, Tabriz Branch, Islamic Azad University, Tabriz, Iran. [3]Sustainable Development Management Research Center of Urmia lake basin, Tabriz Branch, Islamic Azad University, Tabriz, Iran. [4]Department of Chemistry, Ahar Branch, Islamic Azad University, Ahar, Iran. [5]Industrial Nanotechnology Research Center, Tabriz Branch, Islamic Azad University, Tabriz, Iran. ✉email: mehrizad@iaut.ac.ir
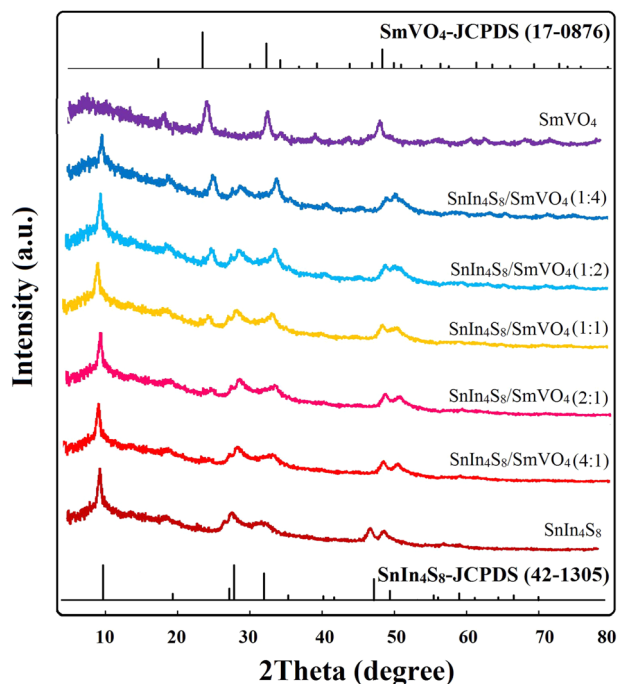
Fig. 1 XRD patterns. SnIn$_4$S$_8$. SmVO$_4$. SnIn$_4$S$_8$/SmVO$_4$.

In the present study, SnIn$_4$S$_8$/SmVO$_4$ photocatalyst was synthesized with a proposed Z-scheme heterojunction to reduce Cr^{6+} and degrade RhB in a visible-light-driven redox process. Since cost and time saving and accurate estimation of results are research priorities, this work aims to design experiments, optimize, and rank operational factors using response surface methodology (RSM) and artificial neural network (ANN), as two multivariate statistics procedures. Furthermore, the kinetics and mechanism of the involved process were studied.

RESULTS AND DISCUSSION

Crystallographic, morphology, and surface area studies

The crystalline structure of the synthesized samples was explored by X-ray diffraction (XRD) patterns depicted in Fig. 1. For bare SnIn$_4$S$_8$, the peaks at 2θ angels of 9.65°, 19.10°, 28.20°, 32.80°, 47.82°, and 49.65° correspond to the (200), (202), (600), (602), (174), and (001) planes of tetragonal phase SnIn$_4$S$_8$, respectively (JCPDS Card No. 42–1305)[1,31]. Similarly, for pure SmVO$_4$, seven peaks appeared at 18.5°, 24.64°, 33.06°, 48.92°, 61.64°, 63.63°, and 69.4°, which are indexed with the (101), (200), (112), (312), (332), (204), and (224) planes of tetragonal phase SmVO$_4$, respectively (JCPDS Card No. 17–0876)[41,42]. In the case of SnIn$_4$S$_8$/SmVO$_4$ samples, predominant diffraction peaks of SnIn$_4$S$_8$ and SmVO$_4$ were observed, confirming the successful formation of SnIn$_4$S$_8$/SmVO4.

The field emission-scanning electron microscope (FE-SEM) images of SmVO$_4$, SnIn$_4$S$_8$, and SnIn$_4$S$_8$/SmVO$_4$ with two magnifications are shown in Fig. 2. According to Fig. 2a, a′, the SmVO$_4$ sample formed of uniform spherical nanoparticles. Fig. 2b, c represent the formation of flower-like SnIn$_4$S$_8$ and SnIn$_4$S$_8$/SmVO$_4$ microspheres. The high-magnification FE-SEM images of SnIn$_4$S$_8$ and SnIn$_4$S$_8$/SmVO$_4$ (Fig. 2b′, c′) reveal that these microspheres were loosely assembled by numerous nanosheets.

The mechanism behind the formation of flower-like morphology was followed through the synthesis of SnIn$_4$S$_8$ at different hydrothermal reaction times. Supplementary Fig. 1 illustrates the FE-SEM images of synthesized samples at different hydrothermal times. As shown in Supplementary Fig. 1a, irregular wrinkled nanosheets with a clinging tendency were formed at 4 h. By
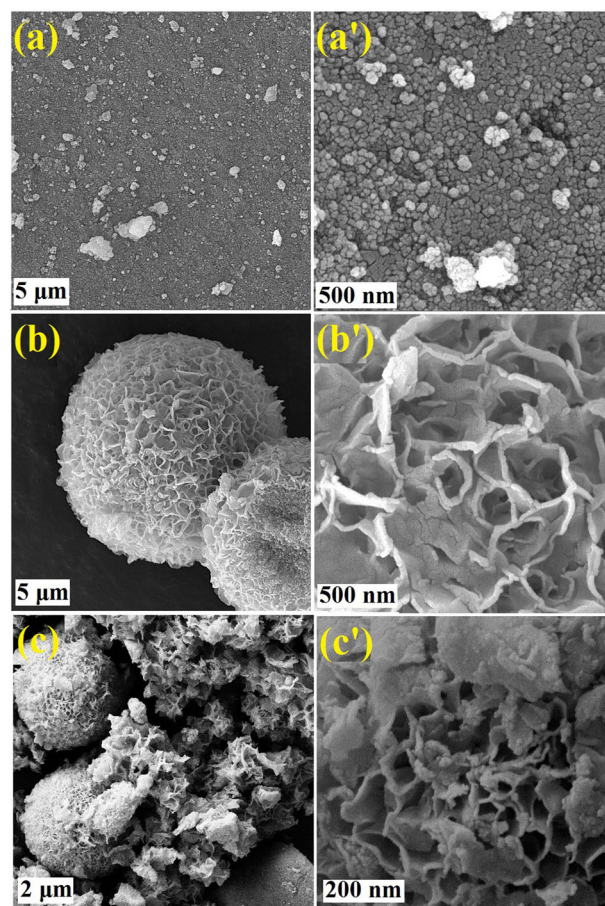

Fig. 2 FE-SEM images. a, a′ SmVO$_4$. **b, b′** SnIn$_4$S$_8$. **c, c′** SnIn$_4$S$_8$/SmVO$_4$.

increasing hydrothermal time to 8 h, the SnIn$_4$S$_8$ hierarchical microspheres begin to form by self-assembling a large number of nanosheets (Supplementary Fig. 1b). When the hydrothermal time prolongs to 12 h, the microspheres obtained from the nanosheets found a more regular arrangement and formed a perfect flower-shaped sphere (Supplementary Fig. 1c).

The constituent elements of the SnIn$_4$S$_8$/SmVO$_4$ composite was unraveled by energy dispersive X-ray (EDX) spectrum (Supplementary Fig. 2). The symmetrical distribution of relevant elements on the surface of the SnIn$_4$S$_8$/SmVO$_4$ composite was depicted well by the EDX elemental mapping (Supplementary Fig. 3).

The microstructure of the binary SnIn$_4$S$_8$/SmVO$_4$ composite was further scrutinized by transmission electron microscope (TEM) images (Supplementary Fig. 4), by which SnIn$_4$S$_8$ nanosheets decorated with SmVO$_4$ nanoparticles are seen. Close contact between composite components aids heterojunction formation, transfer of photoexcited charge carriers, and their separation in photocatalytic processes[8,30,31].

The nitrogen adsorption-desorption curves and Brunauer-Emmett-Teller (BET) analysis results were surveyed to evaluate the surface characteristics of the SnIn$_4$S$_8$, SmVO$_4$, and binary SnIn$_4$S$_8$/SmVO$_4$ composite. As per Fig. 3a, the N$_2$ adsorption-desorption curves of all samples showed a type-IV isotherm with an H3 hysteresis loop (IUPAC classification)[43], indicating the presence of mesopores in the structure of the samples. The obvious hysteresis (0.3–1.0 p/p$_0$) between the adsorption and desorption branches of SnIn$_4$S$_8$/SmVO$_4$ indicates the presence of considerable mesopores in its texture. This hysteresis can be attributed to the voids in the SnIn$_4$S$_8$ hierarchical microsphere. This result was confirmed by calculated pore size distribution ranging 1 to 10 nm from the desorption branch of the Barrett-
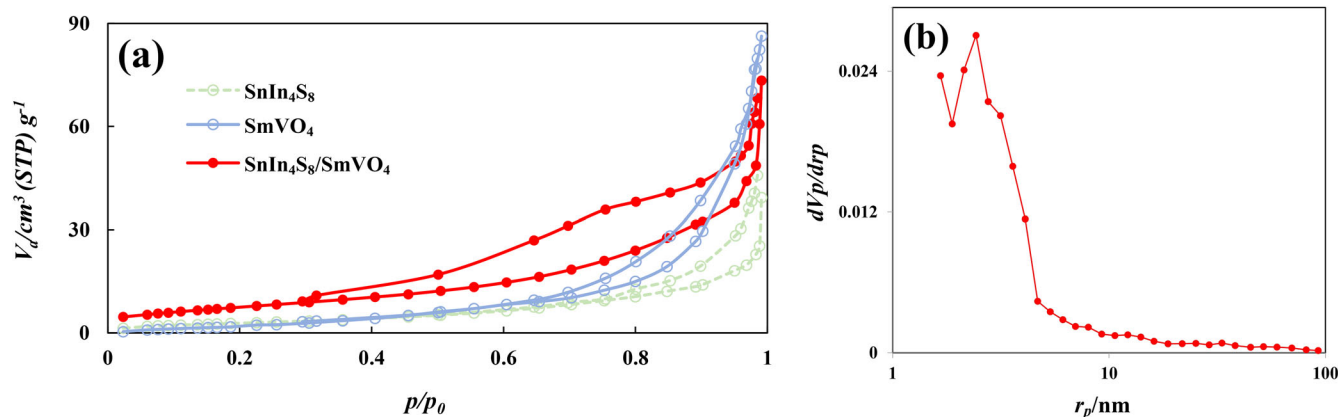
Fig. 3 N$_2$ adsorption-desorption and pore size distribution curves. a N$_2$ adsorption-desorption curves of SnIn$_4$S$_8$, SmVO$_4$, and SnIn$_4$S$_8$/SmVO$_4$. **b** pore size distribution curve of SnIn$_4$S$_8$/SmVO$_4$.

Joyner-Halenda (BJH) plot (Fig. 3b). Besides, the values of the specific surface area of SnIn$_4$S$_8$, SmVO$_4$, and SnIn$_4$S$_8$/SmVO$_4$ were estimated from BET analysis as 17.18, 32.93, and 28.56 m^2 g^{-1}, respectively. Obviously, introducing SmVO$_4$ spherical nanoparticles led to a significant increase in SnIn4S8/SmVO$_4$ specific surface area compared with SnIn$_4$S$_8$ nanosheets. Notably, the obtained specific surface area for SnIn$_4$S$_8$/SmVO$_4$ has an acceptable value compared with its similar binary composites, such as SnIn$_4$S$_8$/Bi$_2$MoO$_6$ (14.3 m^2 g^{-1}), AgInS$_2$/SnIn$_4$S$_8$ (21.7 m^2 g^{-1}), CdS/SnIn$_4$S$_8$ (32.1 m^2 g^{-1}), and g-C$_3$N$_4$/SnIn$_4$S$_8$ (18.7 m^2 g^{-1})[8,23,24,32].

Band gap energy, band edge potentials, and e$^-$-h$^+$ separation studies

The band gap energies (E_g) of synthesized samples were calculated by the UV–Vis diffuse reflectance spectra (Fig. 4a) and Kubelka-Munk function ($F(R) = (1-R)^2/2R$, where R denotes the reflectance value). The E_g can be obtained by drawing a plot of $[F(R)hu]^{1/2}$ versus the photon energy (hu) and extrapolating the plots to $[F(R)hu]^{1/2} = 0$ (Fig. 4b)[44]. The E_g values were determined to be about 2.11, 1.87, and 2.03 eV for SnIn$_4$S$_8$, SmVO$_4$, and SnIn$_4$S$_8$/SmVO$_4$, respectively, thereby guaranteeing their utilization under visible light. In this regard, the introduced SmVO$_4$ reduces the E_g value of SnIn$_4$S$_8$ from 2.11 to 2.03 eV.

The band edge potentials of studied semiconductors were estimated using the Mott-Schottky plots (Fig. 4c) and E_g values. According to Fig. 4c, the slope of the plots is positive, indicating the n-type nature of semiconductors. The flat-band potential (E_{FB}) values of SnIn$_4$S$_8$ and SmVO$_4$ were determined as −0.85 and 0.14 V vs. Ag/AgCl, respectively, by extrapolating the plots to $C^{-2} = 0$. It is of note that the potential of the conduction band (E_{CB}) of an n-type semiconductor is approximately equal to E_{FB} vs. NHE (Normal Hydrogen Electrode), which can be computed from the following empirical formula:

$$E_{CB} \approx E_{FB}(vs.NHE, pH=7) = E_{FB}(vs.Ag/AgCl, pH=6) + E^0(Ag/AgCl) - 0.0591 \tag{1}$$

where $E°(Ag/AgCl) = 0.21$ V (vs. NHE)[45]. Accordingly, the E_{CB} values of SnIn$_4$S$_8$ and SmVO$_4$ were calculated as −0.69 and 0.29 V vs. NHE, respectively. Meanwhile, the valence band potentials (E_{VB}) of SnIn$_4$S$_8$ and SmVO$_4$ were computed as 1.42 and 2.16 V vs. NHE, respectively, using the $E_{VB} = E_{CB} + E_g$ equation.

In the next step, the e$^-$-h$^+$ separation ability of individual and binary samples was explored using the photoluminescence (PL) spectra. A low-intensity PL emission spectrum normally indicates a lower recombination rate of e$^-$-h$^+$, and vice versa[46]. As shown in Fig. 4d, the weakest PL intensity belongs to SnIn$_4$S$_8$/SmVO$_4$, indicating suppression of charge recombination by constructing SnIn$_4$S$_8$/SmVO$_4$ heterojunction. Such a desirable outcome can be attributed to the band structure modulation in heterojunction, which enhances the photocatalytic activity. For detailed explanations, see the mechanism section.

Comparison of the performance of the synthesized powders toward Cr^{6+} and RhB removal

The adsorption and photocatalytic performance of simplex and binary powders were investigated by monitoring the removal of Cr^{6+} and RhB. As shown in Fig. 5, the contribution of Cr^{6+} and RhB adsorption by the synthesized powders was little compared to their photocatalytic removal. Figure 5 also illustrates that all binary SnIn$_4$S$_8$/SmVO$_4$ composites had higher photocatalytic activity than the single-phase component samples under visible light irradiation. As mentioned above, constructing SnIn$_4$S$_8$/SmVO$_4$ heterostructure suppresses e$^-$-h$^+$ recombination and enhances photocatalytic activity. However, the SnIn$_4$S$_8$/SmVO$_4$ composite with an equal molar ratio of components exhibited top-flight photocatalytic performance as compared to other ratios. According to the literature, flower-like structures such as SnIn$_4$S$_8$ have potential photocatalytic applications because of their particular configuration, especially the presence of hierarchical pores. According to Yan et al., the pores inside hierarchical architectures can act as light transmission paths to penetrate photon energy to the depths of the photocatalyst structure, increasing its light-harvesting significantly. In addition, the catalyst photoabsorption improves by increasing the light absorption, reflection, and scattering within such porous architectures. Furthermore, abundant pores in this structure provide numerous active sites for adsorbing more target species[19]. It seems that increasing SmVO$_4$ content in the SnIn$_4$S$_8$/SmVO$_4$ texture from an optimal ratio could shield the SnIn$_4$S$_8$ surface, thereby impeding the light absorption by SnIn$_4$S$_8$ and also blocking the active sites. Therefore, a proper molar ratio of composite components could substantially enhance the photoactivity of the composite. In continuation of our investigation, the role of SnIn$_4$S$_8$/SmVO$_4$ (1:1) toward Cr^{6+} reduction and RhB degradation at visible light exposure was evaluated.

Assessing the role of operational factors and process optimization by RSM

As mentioned in the experimental section, the effect of four influential factors was studied during 30 RSM-designed experiments to find the optimal condition for photocatalytic Cr^{6+} reduction or RhB degradation (Supplementary Tables 1, 2).

After importing the laboratory results to the DX7 software and implementing stepwise command (to remove the insignificant linear, quadratic, and interaction effects), theoretical results were
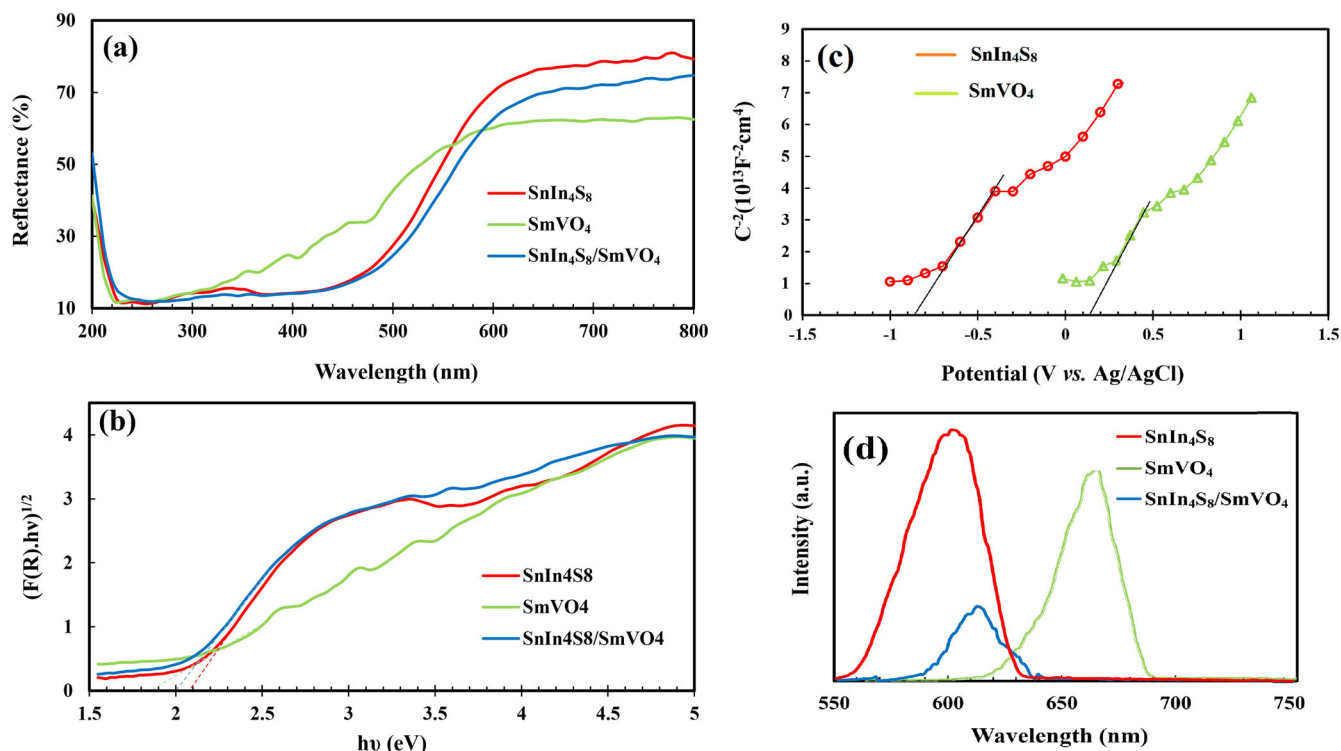
Fig. 4 **Plots of the optical properties of the synthesized samples. a** UV-Vis DRS. **b** $[F(R)h\upsilon]^{1/2}$ versus $h\upsilon$. **c** Mott-Schottky. **d** PL.
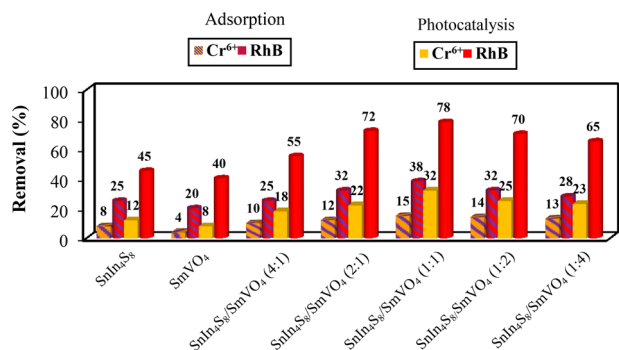

Fig. 5 **Comparison of the adsorption and photocatalytic performance.** Effect of the simplex and binary powders on Cr^{6+} and RhB removal efficiency. ($[Powder]_0$: 0.5 g L^{-1}; $[Cr^{6+}]_0$: 60 mg L^{-1}; $[RhB]_0$: 6 mg L^{-1}; pH: 7; Time: 50 min).

predicted by the following reduced quadratic polynomial equations:

$$
\begin{aligned}
Cr^{6+}\,removal(\%) = {} & 53.20 - 0.61[Cr]_0 + 412.68[Catalyst]_0 - 9.20pH \\
& + 0.71Time + 0.06[Cr]_0.pH - 69.30[Catalyst]_0.pH \\
& - 0.03pH.Time + 2541.08[Catalyst]_0^2 \\
& + 0.38pH^2 - 2.20 \times 10^{-3}Time^2
\end{aligned}
$$
(2)

$$
\begin{aligned}
RhB\,removal(\%) = {} & 115.42 + 0.76[RhB]_0 - 250.01[Catalyst]_0 \\
& - 2.52pH - 0.43Time + 8.75 \times 10^{-3}[RhB]_0.Time \\
& + 15.78[Catalyst]_0.pH + 1.43[Catalyst]_0.Time \\
& + 0.01pH.Time - 0.02[RhB]_0^2 + 1.01 \times 10^{-3}Time^2
\end{aligned}
$$
(3)

The accuracy and precision of the proposed models were assessed by analysis of variance (ANOVA) statistical testing. Statistically, a high F-value and a low p-value (<0.05) indicate

the significance of a model[47]. According to Supplementary Tables 3, 4, the F and p-values of both models at a 95% confidence interval indicate their statistical significance. The lack of fit F-values of models also suggests the lack of fits is not significant relative to the pure error. In addition, the predicted and adjusted R-Squared values close to 1 confirmed the satisfactory correlation between experimental and theoretical removal efficiency values. Furthermore, according to diagnostic plots depicted in Supplementary Figs. 5, 6, the normality of residuals' dispersion (Supplementary Fig. 5), and random errors in runs (Supplementary Fig. 6) indicate the precision of the proposed models. Based on the mentioned points, Eqs. (2) and (3) were satisfactory models for predicting the efficiency of Cr^{6+} and RhB removal.

As mentioned above, running the stepwise command in the DX7 software removes the negligible effects and represents the major linear, quadratic, and mutual effects. As can be seen in Supplementary Table 3 and Eq. (2), the binary interaction of solution pH with the initial Cr^{6+} concentration, catalyst dosage, and irradiation time have pivotal roles in the photocatalytic reduction of Cr^{6+}. These outcomes are graphically illustrated by 3D response surfaces in Fig. 6a–c to interpret these interactions. Similarly, Supplementary Table 4 and Eq. (3) show that interactions of $[RhB]_0*Time$, $[Catalyst]_0*pH$, $[Catalyst]_0*Time$, and $pH*Time$ are major mutual effects in photocatalytic degradation of RhB. The response surfaces of these effects are depicted in Fig. 7a–d.

As shown in Fig. 6a–c, acidic pHs were favorable to the photocatalytic reduction of Cr^{6+}. In this respect, Cr^{6+} exists in forms of $HCrO_4^-$ and $Cr_2O_7^{2-}$ in acidic solutions, and its photocatalytic reduction occurs according to Eqs. (4) and (5)[48,49]. It is noteworthy that the abundance of H^+ is suitable for reducing Cr^{6+}. In alkaline environments, CrO_4^{2-} ion is the dominant species of Cr^{6+}, whose photocatalytic reduction produces $Cr(OH)_3$ precipitation (Eq. (6)). These precipitations cover the catalyst surface, blocking many active sites and hindering photon
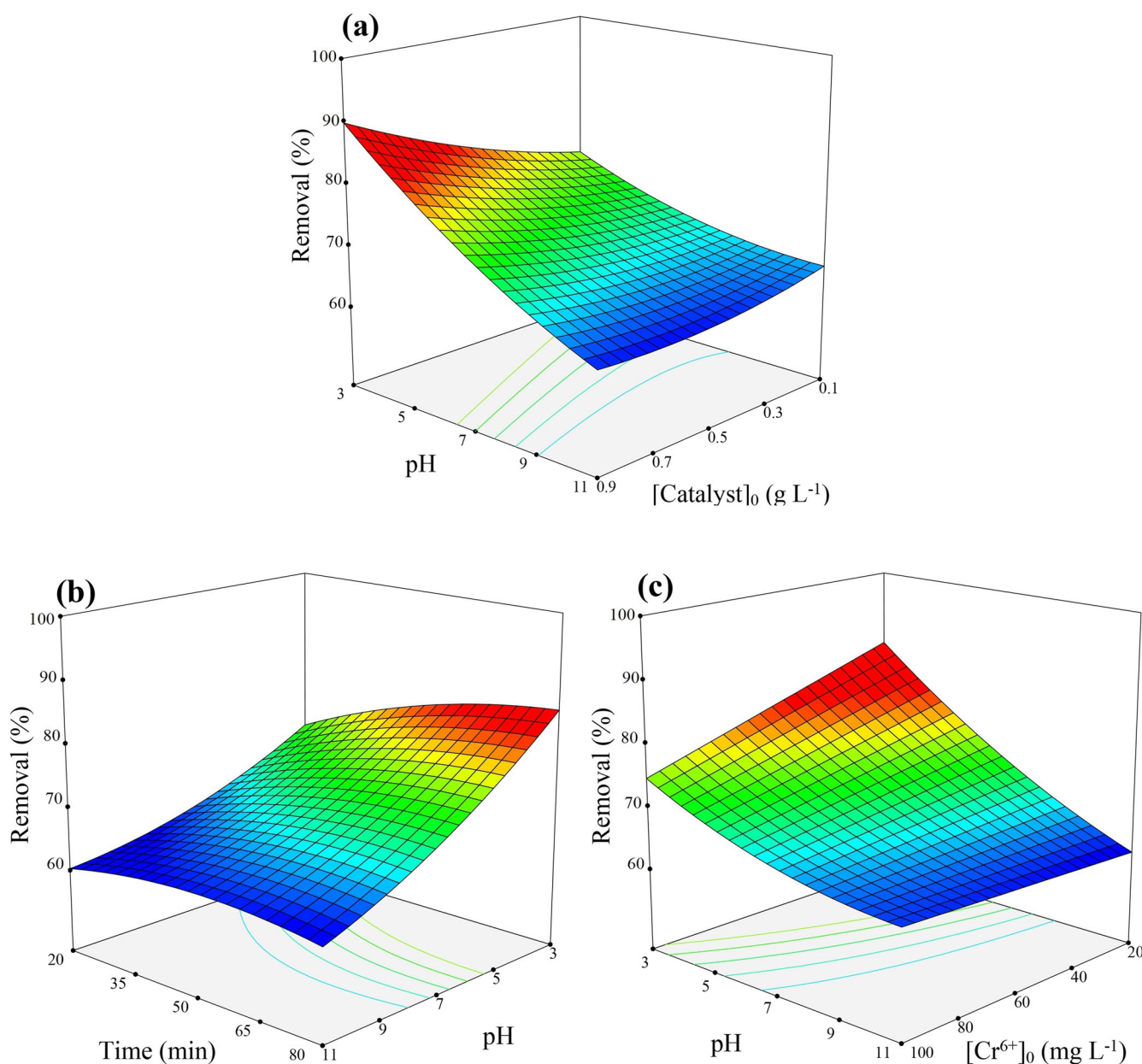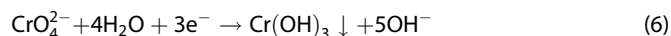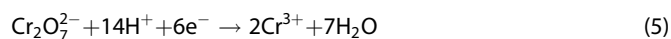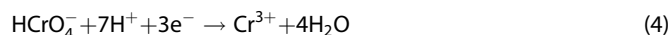
Fig. 6 Response surface plots of the Cr^{6+} removal efficiency. a pH-catalyst dosage. b pH-irradiation time. c pH-initial Cr^{6+} concentration.

penetration[3].

$$HCrO_4^- + 7H^+ + 3e^- \rightarrow Cr^{3+} + 4H_2O \tag{4}$$

$$Cr_2O_7^{2-} + 14H^+ + 6e^- \rightarrow 2Cr^{3+} + 7H_2O \tag{5}$$

$$CrO_4^{2-} + 4H_2O + 3e^- \rightarrow Cr(OH)_3 \downarrow + 5OH^- \tag{6}$$

Furthermore, the point of zero charge (pH$_{pzc}$) of the SnIn$_4$S$_8$/SmVO$_4$ composite is 7.2 (Supplementary Fig. 7), meaning that the composite surface has positively and negatively charged at pHs below and beyond 7.2, respectively. Thus, the electrostatic attraction between HCrO$_4^-$ and Cr$_2$O$_7^{2-}$ with positively charged catalyst surfaces at acidic pHs caused the remarkable adsorption of these anions on the catalyst surface and, thus, substantial photocatalytic reduction of Cr^{6+}. Consequently, the cleanup pathway of Cr^{6+} is more favorable under strong acidic conditions. In Fig. 6a, b, the pH interactions with catalyst dosage and irradiation time show that increasing the catalyst amount and irradiation duration in relatively strong acidic environments increases the efficiency. This enhancement might be due to the increased available active sites and the possibility of creating more active species. Besides, according to Fig. 6c, the removal efficiency was decreased at higher Cr^{6+} concentrations because of huge amounts of Cr^{6+} ions and the non-responsiveness of involved active species[30,31].

According to Fig. 7a–d, increasing the initial dye concentration, catalyst dosage, and duration of irradiation increases the RhB removal efficiency. In fact, all three mentioned factors raise the chance of the RhB molecules' collision with the catalyst surface, thereby increasing the photocatalytic eradication of RhB. Although an increment in dye concentration may prevent the penetration of photons deep inside the solution, it can be compensated by the prolonged illumination time (Fig. 7a). The obtained results are consistent with the results observed in previous studies[44,50,51].

According to Fig. 7b, d, alkaline pHs were favorable to photocatalytic degradation of RhB. Indeed, the electrostatic
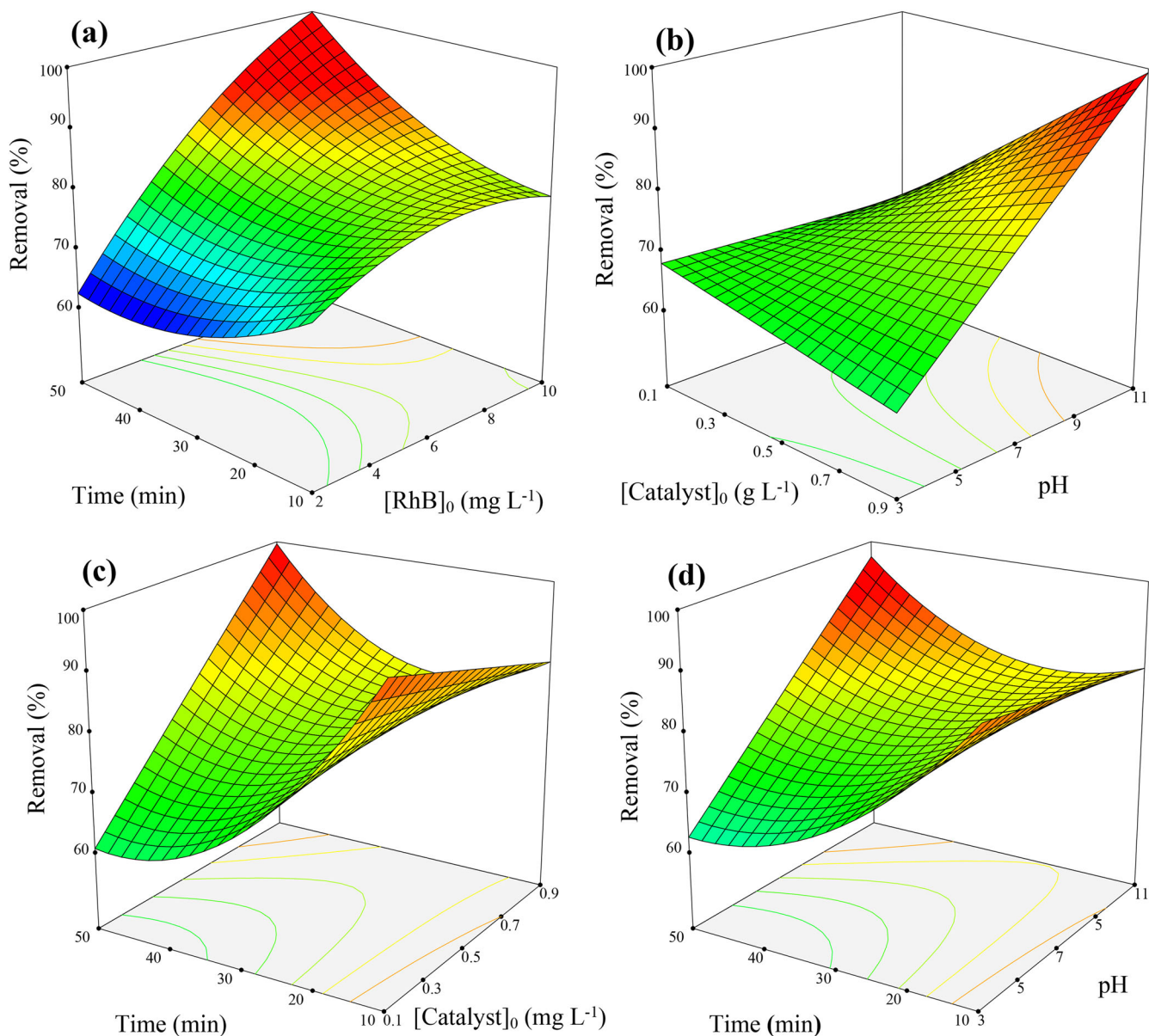
Fig. 7 Response surface plots of the RhB removal efficiency. a irradiation time-initial RhB concentration. **b** catalyst dosage-pH. **c** irradiation time-catalyst dosage. **d** irradiation time-pH.

Table 1. RSM-based optimal conditions for photocatalytic Cr^{6+} reduction and RhB degradation.					
[Pollutant]$_0$ (mg L^{-1})	[Catalyst]$_0$ (g L^{-1})	pH	Time (min)	Removal (%) Pred. (RSM)	Removal (%) Exp.
40 (Cr^{6+})	0.7	3	65	93.25	90.93
8 (RhB)	0.8	9	45	99.09	97.57

attraction between negatively charged catalyst surfaces and cationic molecules of RhB caused the remarkable pulling of RhB toward the catalyst surface at basic pHs, leading to substantial photocatalytic degradation of RhB dye. This conclusion is entirely consistent with the results obtained by other studies[52].

Typically, determining the optimal conditions is the final step in experimental design. Table 1 summarizes the RSM-based optimum conditions for the removal efficiency of Cr^{6+} and RhB.

Figure 8 presents the UV-Vis spectra and photographs of Cr^{6+} and RhB solutions before and after the photocatalytic process. The fading of the solutions' color and a significant decrease in absorbance at the corresponding maximum wavelengths indicate the remarkable photocatalytic removal of Cr^{6+} and RhB under the optimal RSM-based conditions.

The extent of RhB mineralization in the photocatalytic process was estimated using a total organic carbon (TOC) analyzer (Shimadzu TOC-L-CPN). The obtained results demonstrate that TOC was removed up to 73.98% at optimal RSM-based conditions, suggesting effective mineralization of RhB dye. In addition, the produced by-products during the RhB degradation were identified by gas chromatography-mass spectrometry (GC-MS) according to the instructions reported in the Supplementary Methods. The GC chromatogram of degraded RhB and corresponding Mass spectra are presented in Supplementary Figs. 8, 9, respectively. Figure 9 illustrates the chemical structure of 7 by-products produced during RhB photocatalytic degradation. These compounds'

appearance confirmed the remarkable degradation of RhB dye through the SnIn$_4$S$_8$/SmVO$_4$ photocatalyzed process.

Process re-optimization and ranking of operational factors by ANN

The operational factors were ranked, and the process was re-optimized using the ANN approach. As mentioned in the experimental section, 30 experiments were designed by RSM and laboratory results were normalized and imported to the MATLAB software as input and output data, respectively. The process was modeled using a two-layer feed-forward/back-

Fig. 8 UV-Vis spectra and photographic images (before and after photocatalysis). a Cr^{6+} solution. **b** RhB solution.

propagation network. Here, the Sigmoid and Purlin functions were used as activation functions and the Levenberg-Marquardt as the training algorithm. Networks with various numbers of hidden neurons were tried to find the optimum network. Generally, a network with an appropriate number of hidden neurons has the least mean square error (MSE)[53]. In Supplementary Fig. 10, networks with 8 and 10 hidden neurons had the least MSE in ANN modeling of Cr^{6+} reduction and RhB degradation, respectively. The accuracy and precision of the selected networks were assessed by correlation coefficient (R) values of graphs of training, validation, test, and total data (Supplementary Figs. 11, 12). All plots exhibit R values close to unity, indicating the networks would cover the data well enough. This result is supported by congruence between experimental and ANN-predicted removal efficiency values listed in Supplementary Tables 1, 2.

After validating the prepared ANNs, the operational factors were ranked using the connection weights of the networks listed in Supplementary Tables 5, 6 and Garson's equation (Supplementary Equation 4). The relative importance of operational factors is illustrated by pie charts in Supplementary Fig. 13. As shown in Supplementary Fig. 13a, b, all factors are effective in photocatalytic Cr^{6+} reduction and RhB degradation, but pH is more important factor.

Finally, the performance of RSM and ANN multivariate statistics procedures was compared in modeling the photocatalytic process. According to Supplementary Fig. 14, both approaches have a good capability to predict the removal efficiency; however, a closer look reveals that ANN's model can explain the process behavior more accurately and reliably than RSM because of its broader capabilities.

Mechanism of the photocatalytic process

Light-harvesting ability, a sufficient lifetime of photoinduced e⁻-h⁺ pairs, and sufficient redox ability are three main determinants of photocatalytic performance. A narrow bandgap photocatalyst is desirable for excitation with cost-effective irradiation sources like visible light. Although a photocatalyst with a high CB and low VB (i.e., a wide bandgap photocatalyst) plays a critical role in achieving a high redox ability, these two conditions are contradictory.

The design of heterojunction photocatalysts is among the promising methods to overcome the mentioned problems. Based
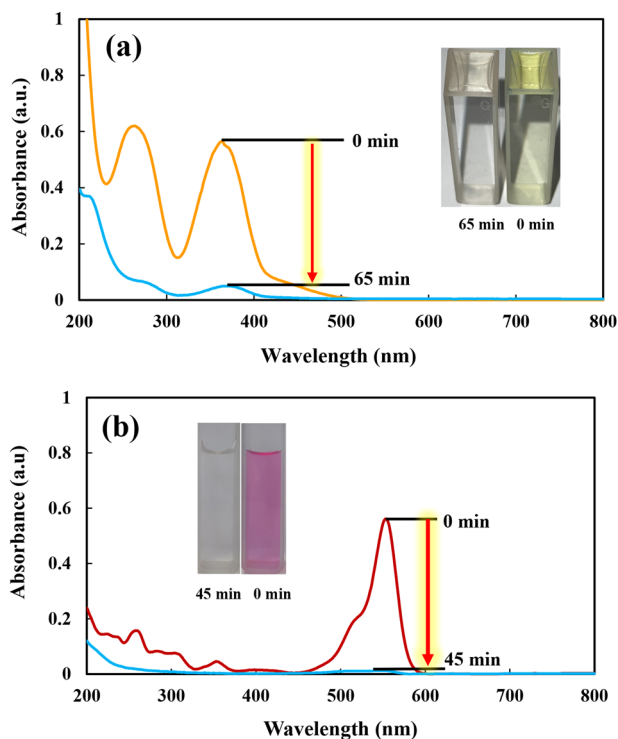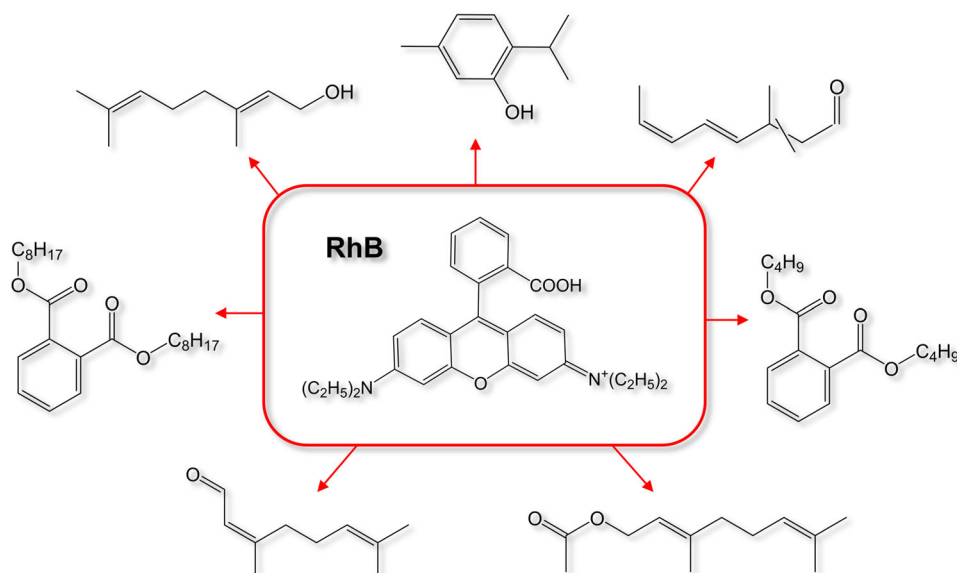
Fig. 9 Detected by-products. Produced by-products during the RhB degradation.
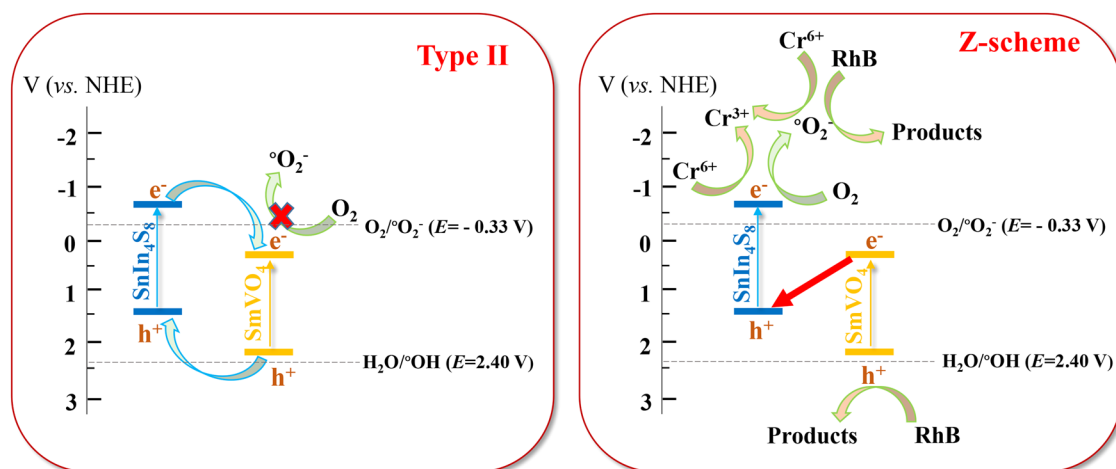
Fig. 10 Mechanism of the photocatalytic process. Two default configuration for studied heterojunction photocatalyst.

on the position of the CB and VB of the involved semiconductors or depending on their types (*n* or *p*-type), the architecture of heterojunction photocatalysts is divided into five categories, which is abundantly reported in the literature: Type-I heterojunction, Type-II heterojunction, *p*-*n* junction, Schottky junction, and Z-scheme heterojunction. Notably, there are two main types of Z-scheme heterojunctions, namely direct Z-scheme (without any electron mediator) and indirect Z-scheme (with an electron mediator)[54–56].

Typically, two important steps to provide the architecture of a heterojunction photocatalyst are: determining the band alignment of involved semiconductors and figuring out the involved active species. Based on the above Mott-Schottky and UV-Vis DRS analysis, the CB and VB potentials were determined as −0.69 and 1.42 V for $SnIn_4S_8$ and 0.29 and 2.16 V for $SmVO_4$, respectively. Supplementary Fig. 15a depicts the relative position of the band edge potential of mentioned semiconductors. Besides, clarifying the active species was followed by trapping tests under RSM-based optimal conditions. Ascorbic acid (AA), tert-butanol (TB), potassium bromate (PB), and ethylene diamine tetra-acetic acid (EDTA) were used as scavenging agents of superoxide radicals ($^\bullet O_2^-$), hydroxyl radicals ($^\bullet OH$), photoinduced electrons (e^-), and holes (h^+), respectively. As displayed in Supplementary Fig. 15b, Cr^{6+} reduction was significantly declined by suppressing $^\bullet O_2^-$ and e^- in the presence of AA and PB; meanwhile, RhB removal efficiency was reduced by quenching $^\bullet O_2^-$ and h^+ in the presence of AA and EDTA, respectively. In short, superoxide radicals and photoinduced electrons and holes played vital roles in the photocatalytic removal of Cr^{6+} and RhB under visible light irradiation.

To realize the architecture of the studied heterojunction photocatalyst, two configurations in Fig. 10 were regarded as defaults.
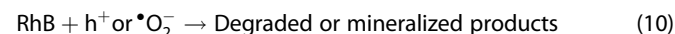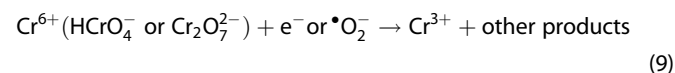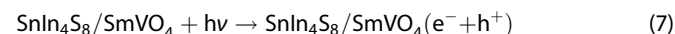
The E_g values of $SnIn_4S_8$ and $SmVO_4$ indicate that their exposure to visible light leads to the transfer of photoinduced electrons from the VB to the CB of each of them, maintaining the holes on their VB. The trapping tests also demonstrated that $^\bullet O_2^-$, e^-, and h^+ are dominant species in the photocatalytic redox reactions.

Since the CB potential of $SmVO_4$ was more positive than the standard potential of $^\bullet O_2^-/O_2$ (−0.33 V *vs*. NHE)[57], the hypothesis of photogenerated electrons transmission from $SnIn_4S_8$-CB to $SmVO_4$-CB and, $^\bullet O_2^-$ production by accumulated electrons in $SmVO_4$-CB is rejected. Hence, the formation of type-II heterojunction between $SnIn_4S_8$ and $SmVO_4$ through the electrons migration from $SnIn_4S_8$-CB to $SmVO_4$-CB simultaneous with the transfer of holes from $SmVO_4$-VB to $SnIn_4S_8$-VB is far from the expected. Alternatively, the CB potential of $SnIn_4S_8$ was negative enough

compared with the standard potential of $^\bullet O_2^-/O_2$; thus, the adsorbed O_2 molecules on the catalyst surface could be reduced to $^\bullet O_2^-$ by electron injection from the $SnIn_4S_8$-CB. Such an approach can be possible through e^--h^+ recombination between the CB of $SmVO_4$ and VB of $SnIn_4S_8$. Accordingly, the electrons and holes remain on the CB of $SnIn_4S_8$ and VB of $SmVO_4$, respectively. As mentioned, gathered electrons on $SnIn_4S_8$-CB could reduce O_2 to yield $^\bullet O_2^-$ to participate in the photocatalytic removal of pollutants. It is of note that the VB potential of $SmVO_4$ was not positive enough compared with the standard potential of $H_2O/^\bullet OH$ (+2.40 V *vs*. NHE)[58]. Therefore, the adsorbed H_2O molecules on the catalyst surface could not produce hydroxyl radicals. Hence, collected holes on $SmVO_4$-VB would directly participate in the photocatalytic removal of pollutants. This finding is consistent with the trapping test results.

Based on the mentioned points, photocatalytic Cr^{6+} reduction and RhB degradation were taken by superoxide radicals and electron-holes by establishing a direct Z-scheme heterojunction between $SnIn_4S_8$ and $SmVO_4$ under visible light irradiation.

Accordingly, the plausible reactions during the photocatalytic Cr^{6+} reduction and RhB degradation through the Z-scheme heterojunction of $SnIn_4S_8/SmVO_4$ under RSM-based optimal conditions were assessed. Since the CB potential of $SnIn_4S_8$ was more negative than the standard reduction potential of Cr^{6+}/Cr^{3+} (1.33 V *vs*. NHE)[59], Cr^{6+} could be reduced to Cr^{3+} by photoinduced electrons. In addition, superoxide anion radicals could reduce Cr^{6+} to Cr^{3+}. Besides, RhB could be oxidized and reduced by photoinduced holes and superoxide anion radicals, respectively. According to the mentioned points and based on the related literature, the following reactions are expected in the involved process:

$$SnIn_4S_8/SmVO_4 + hv \rightarrow SnIn_4S_8/SmVO_4(e^- + h^+) \qquad (7)$$

$$O_2 + e^- \rightarrow {}^\bullet O_2^- \qquad (8)$$

$$Cr^{6+}(HCrO_4^- \text{ or } Cr_2O_7^{2-}) + e^- \text{ or } {}^\bullet O_2^- \rightarrow Cr^{3+} + \text{other products}$$
$$\qquad (9)$$

$$RhB + h^+ \text{or} {}^\bullet O_2^- \rightarrow \text{Degraded or mineralized products} \qquad (10)$$

Reusability test and kinetics study

Catalyst recovery and reuse are vital in its practical applications. Hence, the catalyst reusability was tested under RSM-based optimal conditions, according to the method described in the Supplementary Methods. As it is clear from Supplementary Fig. 16a,

Table 2. Photocatalytic Cr^{6+} reduction over various photocatalysts under visible light irradiation.

Catalyst	k_{app} (min^{-1})	Photocatalytic degradation	Refs.
rGO/SnIn$_4$S$_8$	0.018	67.00% within 30 min	ref. [62]
Bi$_{.333}$(Bi$_6$S$_9$)Br	0.023	90.96% within 60 min	ref. [63]
Bi$_{3.25}$La$_{0.75}$Ti$_3$O$_{12}$	Not given	97.10% within 150 min	ref. [64]
In$_2$O$_3$@SnIn$_4$S$_8$	0.035	99.40% within 90 min	ref. [65]
SnIn$_4$S$_8$/CeO$_2$	0.047	98.8% within 75 min	ref. [31]
SnIn$_4$S$_8$/SmVO$_4$	0.036	90.93% within 65 min	This work

Table 3. Photocatalytic RhB reduction over various photocatalysts under visible light irradiation.

Catalyst	k_{app} (min^{-1})	Photocatalytic degradation	Refs.
NiFe$_2$O$_4$/MIL-53(Fe)	0.016	95.00% within 180 min	ref. [66]
TiO$_2$/ZrO$_2$	Not given	99.00% within 180 min	ref. [52]
Ag-BaTiO$_3$	Not given	83.00% within 75 min	ref. [67]
WO$_3$/rGO/SnIn$_4$S$_8$	0.085	98.50% within 60 min	ref. [68]
TiO$_2$ -GO-AgNs	0.031	93.00% within 300 min	ref. [69]
SnIn$_4$S$_8$/SmVO$_4$	0.080	97.57% within 45 min	This work

the ability to use the recovered catalyst can be justified up to four times. However, more reuse is not reasonable, probably due to blocking active sites or unavoidable loss of SnIn$_4$S$_8$/SmVO$_4$ powders during the repetitive tests[60]. Supplementary Fig. 16b shows the XRD patterns of fresh and recycled photocatalysts. As can be seen, the XRD diffraction peaks of SnIn$_4$S$_8$/SmVO$_4$ photocatalysts remain the same as that of fresh SnIn$_4$S$_8$/SmVO$_4$ after four runs. In addition, comparing the FE-SEM images of fresh and recycled photocatalysts (Supplementary Fig. 17) indicates that no noticeable change occurred in SnIn$_4$S$_8$/SmVO$_4$ composite morphology after four consecutive uses. These results suggest the photostability and reusability of the SnIn$_4$S$_8$/SmVO$_4$ as a photocatalyst from the practical aspect.

Studying the kinetics of photocatalytic processes is another important aspect in proving their applicability. The literature review indicates that Langmuir-Hinshelwood's pseudo-first-order model is the most likely kinetics model for describing photo-degradation processes (see the detailed explanations of this model in the Supplementary Methods). Hence, this model was studied in the present research under RSM-based optimal conditions. As can be inferred from Supplementary Fig. 18, the experimental data for both Cr^{6+} and RhB dye were consistent with the pseudo-first-order kinetics model (R^2 values close to one) with the apparent rate constants (k_{app}) of 0.036 and 0.080 min^{-1}, respectively.

The advantages of the prepared SnIn$_4$S$_8$/SmVO$_4$ heterojunction were studied by comparing its photocatalytic performance for Cr^{6+} reduction and RhB degradation with recently published other photocatalysts. According to Tables 2 and 3, the obtained removal efficiency values in this study are quite comparable with other photocatalysts. These results indicate that the synthesized SnIn$_4$S$_8$/SmVO$_4$ heterojunction could be considered a prominent visible-light-driven photocatalyst to control organic and inorganic pollutants.

METHODS
The chemical materials, characterization methods, and the methods of the point of zero charge (pH$_{pzc}$) determination and Mott-Schottky tests are provided in the Supplementary Methods.

Preparation of SnIn$_4$S$_8$/SmVO$_4$
The SnIn$_4$S$_8$/SmVO$_4$ composite was prepared as follows:

Synthesis of SnIn$_4$S$_8$. The SnIn$_4$S$_8$ was synthesized via a solvothermal procedure proposed in the literature[1]. Firstly, 0.438 g (1.25 mmol) of SnCl$_4$.5H$_2$O and 1.466 g (5 mmol) of InCl$_3$.4H$_2$O were dissolved in 150 mL of C$_2$H$_5$OH under magnetic stirring at room temperature. Then, 0.939 g (12.5 mmol) of CH$_3$CSNH$_2$ was added to the above solution, and the mixture was further stirred until a uniformly dispersed solution was formed. The obtained blend was transferred into a 250 mL Teflon-lined autoclave and hold on 160 °C for 12 h. The final product was

achieved by centrifuging, rinsing thrice with ethanol and deionized water, and drying at 60 °C for 8 h.

Synthesis of SmVO$_4$. The SmVO$_4$ was synthesized by precipitation method with an equal molar ratio of Sm:V[36]. Firstly, 0.5 g of Sm(NO$_3$)$_2$.6H$_2$O (A) and 0.132 g of NH$_4$VO$_3$ (B) were separately dissolved in 50 mL of deionized water and stirred for 30 min at room temperature. Then, solution B was dropwise added into a round-bottom flask containing solution A under vigorously stirring, whiles the pH of the mixture was kept at 7–8 using NH$_3$. The mixture was stirred for another 2 h. Afterwards, the precipitates were collected centrifugally and rinsed with deionized water to neutrality. The obtained product was oven-dried at 100 °C for 12 h, and calcined in the furnace for 2 h at 500 °C.

Preparation of SnIn$_4$S$_8$/SmVO$_4$. The SnIn$_4$S$_8$/SmVO$_4$ binary composite was synthesized hydrothermally at variable molar ratios of SnIn$_4$S$_8$:SmVO$_4$ (4:1, 2:1, 1:1, 1:2, and 1:4)[37]. Firstly, certain amounts of SnIn$_4$S$_8$ and SmVO$_4$ were separately dispersed in 100 mL of deionized water under ultrasonication at room temperature. Then, both suspensions were transferred into a 250 mL Teflon-lined autoclave to be heated at 120 °C for 8 h. The final product was obtained by centrifuging, rinsing with deionized water, and drying at 80 °C for 8 h.

Designing the photocatalytic experiments, RSM, and ANN modeling of the process
The photocatalytic experiments were conducted under a 300 W halogen lamp irradiation based on the method described in the Supplementary Methods. Supplementary Fig. 19 illustrates the photocatalytic experimental setup.

The experiments were designed using the response surface methodology (RSM) to reduce costs, save time, and obtain optimal conditions. The design and optimization processes were performed using the RSM-based central composite design (CCD) toolbox of the Design-Expert® Version 7 (DX7) package. After preliminary trials (Supplementary Figs. 20, 21), factors contributed were selected at five levels, and the software suggested 30 experiments (Supplementary Tables 1, 2). After conducting the laboratory tests and importing the experimental results to the DX7 software, theoretical results were predicted by a quadratic polynomial equation, Supplementary Equation 2.

Operational factors were ranked and re-optimized by modeling in MATLAB R2020 b software based on the artificial neural network (ANN) toolbox. The mentioned 30 experiments were designed by RSM, and laboratory results were normalized by Supplementary Equation 3. In the next step, they were imported into the software as input and output data, respectively. The photocatalytic process was modeled using a two-layer feed-forward/back-propagation network. After selecting a network with a suitable topology, the operational factors were ranked using the connection weights and Garson's equation, Supplementary Equation 4[61]. For more

information, see the detailed explanations in the Supplementary Methods.

REFERENCES

1. Wang, L. et al. Efficient photocatalytic reduction of aqueous Cr (VI) over flower-like SnIn4S8 microspheres under visible light illumination. *J. Hazard. Mater.* **244**, 681–688 (2013).
2. Chen, D. et al. Fabrication of Bi modified Bi2S3 pillared g-C3N4 photocatalyst and its efficient photocatalytic reduction and oxidation performances. *Appl. Surf. Sci.* **426**, 427–436 (2017).
3. Lu, D. et al. Solvothermal-assisted synthesis of self-assembling TiO2 nanorods on large graphitic carbon nitride sheets with their anti-recombination in the photocatalytic removal of Cr (VI) and rhodamine B under visible light irradiation. *Nanoscale* **9**, 3231–3245 (2017).
4. Zhang, L. et al. One-step in situ synthesis of CdS/SnO2 heterostructure with excellent photocatalytic performance for Cr (VI) reduction and tetracycline degradation. *Chem. Eng. J.* **352**, 863–875 (2018).
5. Ou, B., Wang, J., Wu, Y., Zhao, S. & Wang, Z. Efficient removal of Cr (VI) by magnetic and recyclable calcined CoFe-LDH/g-C3N4 via the synergy of adsorption and photocatalysis under visible light. *Chem. Eng. J.* **380**, 122600 (2020).
6. Cui, H., Dong, S., Wang, K., Luan, M. & Huang, T. Synthesis of a novel Type-II In2S3/Bi2MoO6 heterojunction photocatalyst: Excellent photocatalytic performance and degradation mechanism for Rhodamine B. *Sep. Purif. Technol.* **255**, 117758 (2021).
7. Weng, R. et al. Efficient mineralization of TBBPA via an integrated photocatalytic reduction/oxidation process mediated by MoS2/SnIn4S8 photocatalyst. *Chemosphere* **285**, 131542 (2021).
8. Wang, Z. et al. Novel core-shell SnIn4S8@ Bi2MoO6 heterojunction with highly-enhanced photocatalytic activity for visible light-driven Cr (VI) reduction. *Appl. Surf. Sci.* **589**, 152888 (2022).
9. Mehrizad, A. & Gharbani, P. Novel ZnS/Carbon Nanofiber Photocatalyst for Degradation of Rhodamine 6G: Kinetics Tracking of Operational Parameters and Development of a Kinetics Model. *Photochem. Photobiol.* **93**, 1178–1186 (2017).
10. Qu, X., Alvarez, P. J. J. & Li, Q. Applications of nanotechnology in water and wastewater treatment. *Water Res* **47**, 3931–3946 (2013).
11. Bolisetty, S., Peydayesh, M. & Mezzenga, R. Sustainable technologies for water purification from heavy metals: review and analysis. *Chem. Soc. Rev.* **48**, 463–487 (2019).
12. Ghernaout, D. & Elboughdiri, N. Advanced oxidation processes for wastewater treatment: facts and future trends. *Open Access Lib* **7**, 1–15 (2020).
13. Tabatabaei, S. M., Dastmalchi, S., Mehrizad, A. & Gharbani, P. Enhancement of 4-nitrophenol ozonation in water by nano ZnO catalyst. *Iran. J. Environ. Health Sci. Eng.* **8**, 363–372 (2011).
14. Mehrizad, A. & Gharbani, P. Decontamination of 4-chloro-2-nitrophenol from aqueous solution by graphene adsorption: Equilibrium, kinetic, and thermodynamic studies. *Pol. J. Environ. Stud.* **23**, 2111–2116 (2014).
15. Belver, C., Bedia, J., Gómez-Avilés, A., Peñas-Garzón, M. & Rodriguez, J. J. Semiconductor photocatalysis for water purification. in *Nanoscale materials in water purification* 581–651 (Elsevier, 2019).
16. Tahir, M. B. et al. Advances in photo-catalysis approach for the removal of toxic personal care product in aqueous environment. *Environ. Dev. Sustain.* **22**, 6029–6052 (2020).
17. Wang, H. et al. A review on heterogeneous photocatalysis for environmental remediation: From semiconductors to modification strategies. *Chinese J. Catal.* **43**, 178–214 (2022).
18. Ataei, A., Mehrizad, A. & Zare, K. Photocatalytic degradation of cefazoline antibiotic using zeolite-supported CdS/CaFe2O4 Z-scheme photocatalyst: Optimization and modeling of process by RSM and ANN. *J. Mol. Liq.* **328**, 115476 (2021).
19. Yan, T., Li, L. & Li, G. Solvothermal synthesis of hierarchical SnIn4S8 microspheres and their application in photocatalysis. *Res. Chem. Intermed.* **37**, 297–307 (2011).
20. Yan, T. et al. Porous SnIn4S8 microspheres in a new polymorph that promotes dyes degradation under visible light irradiation. *J. Hazard. Mater.* **186**, 272–279 (2011).
21. Wang, T., Zhang, Y. & Ding, T. One-step solvothermal synthesis of SnIn4S8/TiO2 nanocomposite with enhanced visible-light-activated photocatalytic activity. *Mater. Lett.* **123**, 153–155 (2014).
22. Deng, F. et al. Facile low-temperature co-precipitation method to synthesize hierarchical network-like g-C3N4/SnIn4S8 with superior photocatalytic performance. *J. Mater. Sci.* **51**, 6998–7007 (2016).
23. Deng, F. et al. One-step hydrothermal fabrication of visible-light-responsive AgInS2/SnIn4S8 heterojunction for highly-efficient photocatalytic treatment of organic pollutants and real pharmaceutical industry wastewater. *Appl. Catal. B* **219**, 163–172 (2017).
24. Deng, F. et al. One-step in situ hydrothermal fabrication of octahedral CdS/SnIn4S8 nano-heterojunction for highly efficient photocatalytic treatment of nitrophenol and real pharmaceutical wastewater. *J. Hazard. Mater.* **340**, 85–95 (2017).
25. Lu, M. et al. Construction of cobalt phthalocyanine sensitized SnIn4S8/g-C3N4 composites with enhanced photocatalytic degradation and hydrogen production performance. *Synth. Met.* **268**, 116480 (2020).
26. Guo, H. et al. Construction of direct Z-scheme AgI/Bi2Sn2O7 nanojunction system with enhanced photocatalytic activity: accelerated interfacial charge transfer induced efficient Cr (VI) reduction, tetracycline degradation and Escherichia coli inactivation. *ACS Sustain. Chem. Eng.* **6**, 8003–8018 (2018).
27. Zhu, Z. et al. Fabrication of magnetically recoverable photocatalysts using g-C3N4 for effective separation of charge carriers through like-Z-scheme mechanism with Fe3O4 mediator. *Chem. Eng. J.* **331**, 615–625 (2018).
28. Wang, T. et al. A Z-scheme TiO2 quantum dots fragment-Bi12TiO20 composites for enhancing photocatalytic activity. *Renew. Energy* **147**, 856–863 (2020).
29. Shi, H. et al. Highly efficient visible light driven photocatalytic inactivation of E. coli with Ag QDs decorated Z-scheme Bi2S3/SnIn4S8 composite. *Appl. Catal. B* **254**, 403–413 (2019).
30. Zhang, S. et al. In-situ constructing of one-dimensional SnIn4S8-CdS core-shell heterostructure as a direct Z-scheme photocatalyst with enhanced photocatalytic oxidation and reduction capabilities. *Appl. Surf. Sci.* **542**, 148618 (2021).
31. Shen, C.-H. et al. Efficient photocatalytic H2 evolution and Cr (VI) reduction under visible light using a novel Z-scheme SnIn4S8/CeO2 heterojunction photocatalysts. *J. Hazard. Mater.* **416**, 126217 (2021).
32. Tang, C. et al. Spatially distributed Z-scheme heterojunction of g-C3N4/SnIn4S8 for enhanced photocatalytic hydrogen production and pollutant degradation. *Appl. Surf. Sci.* **598**, 153870 (2022).
33. Yi, M., Park, S.-K., Seong, C.-Y., Piao, Y. & Yu, T. The general synthesis and characterization of rare earth orthovanadate nanocrystals and their electrochemical applications. *J. Alloys Compd.* **693**, 825–831 (2017).
34. Ge, X., Zhang, Y., Wu, H., Zhou, M. & Lin, T. SmVO4 nanocrystals with dodecahedral shape: Controlled synthesis, growth mechanism and photoluminescent properties. *Mater. Res. Bull.* **97**, 81–88 (2018).
35. He, Y. et al. Photodegradation of organics over a new composite catalyst V2O5/SmVO4. *Catal. Commun.* **10**, 1354–1357 (2009).
36. Li, T. et al. Synthesis, characterization and photocatalytic activity of visible-light plasmonic photocatalyst AgBr-SmVO4. *Appl. Catal. B* **138**, 95–103 (2013).
37. Li, T. et al. Synthesis of g-C3N4/SmVO4 composite photocatalyst with improved visible light photocatalytic activities in RhB degradation. *Appl. Catal. B* **129**, 255–263 (2013).
38. Eghbali-Arani, M., Sobhani-Nasab, A., Rahimi-Nasrabadi, M. & Pourmasoud, S. Green synthesis and characterization of SmVO4 nanoparticles in the presence of carbohydrates as capping agents with investigation of visible-light photocatalytic properties. *J. Electron. Mater.* **47**, 3757–3769 (2018).
39. Shandilya, P. et al. Fabrication of fluorine doped graphene and SmVO4 based dispersed and adsorptive photocatalyst for abatement of phenolic compounds from water and bacterial disinfection. *J. Clean. Prod.* **203**, 386–399 (2018).
40. Chen, J. et al. One-step MOF assisted synthesis of SmVO4 nanorods for photocatalytic degradation of tetracycline under visible light. *Mater. Lett.* **276**, 128213 (2020).
41. Leeladevi, K., Kumar, J. V., Arunpandian, M., Thiruppathi, M. & Nagarajan, E. R. Investigation on photocatalytic degradation of hazardous chloramphenicol drug and amaranth dye by SmVO4 decorated g-C3N4 nanocomposites. *Mater. Sci. Semicond. Process.* **123**, 105563 (2021).
42. Quach, T.-A. et al. Direct Z-scheme mediated SmVO4/UiO-66-NH2 heterojunction nanocomposite for the degradation of antibiotic tetracycline hydrochloride molecules under sunlight. *Chemosphere* **303**, 134861 (2022).
43. Rouquerol, J., Rouquerol, F., Llewellyn, P., Maurin, G. & Sing, K. S. W. Adsorption by powders and porous solids: principles, methodology and applications. (Academic press, 2013).
44. Hemmatpour, P. & Nezamzadeh-Ejhieh, A. A Z-scheme CdS/BiVO4 photocatalysis towards Eriochrome black T: An experimental design and mechanism study. *Chemosphere* **307**, 135925 (2022).
45. Zuo, G., Wang, Y., Teo, W. L., Xian, Q. & Zhao, Y. Direct Z-scheme TiO2–ZnIn2S4 nanoflowers for cocatalyst-free photocatalytic water splitting. *Appl. Catal. B* **291**, 120126 (2021).
46. Liu, H. et al. Preparation and photocatalytic activity of Gd3+-doped trititanate nanotubes. *Micropor. Mesopor. Mat.* **142**, 439–443 (2011).

47. Bezerra, M. A., Santelli, R. E., Oliveira, E. P., Villar, L. S. & Escaleira, L. A. Response surface methodology (RSM) as a tool for optimization in analytical chemistry. *Talanta* **76**, 965–977 (2008).

48. Wang, D. et al. In situ construction efficient visible-light-driven three-dimensional Polypyrrole/Zn$_3$In$_2$S$_6$ nanoflower to systematically explore the photoreduction of Cr (VI): Performance, factors and mechanism. *J. H. Mater.* **384**, 121480 (2020).

49. Li, Y.-X., Han, Y.-C. & Wang, C.-C. Fabrication strategies and Cr (VI) elimination activities of the MOF-derivatives and their composites. *Chem. Eng. J.* **405**, 126648 (2021).

50. Khairnar, S. D., Patil, M. R. & Shrivastava, V. S. Hydrothermally synthesized nanocrystalline Nb$_2$O$_5$ and its visible-light photocatalytic activity for the degradation of congo red and methylene blue. *Iran. J. Catal.* **8**, 143–150 (2018).

51. Chaker, H., Ferouani, G., Chikhi, I., Djennas, M. & Fourmentin, S. A novel statistical approach for the synthesis of Chalcones viaClaisen-Schmidt condensation catalyzed by Pd nanoparticles modified mesoporous TiO$_2$ as an efficient heterogeneous catalyst. *Colloid Interface Sci. Commun* **43**, 100461 (2021).

52. Abdi, J., Yahyanezhad, M., Sakhaie, S., Vossoughi, M. & Alemzadeh, I. Synthesis of porous TiO$_2$/ZrO$_2$ photocatalyst derived from zirconium metal organic framework for degradation of organic pollutants under visible light irradiation. *J. Environ. Chem. Eng.* **7**, 103096 (2019).

53. Behnajady, M. A., Eskandarloo, H. & Eskandarloo, F. Artificial neural network modeling of the influence of sol–gel synthesis variables on the photocatalytic activity of TiO$_2$ nanoparticles in the removal of Acid Red 27. *Res. Chem. Intermed.* **41**, 6463–6476 (2015).

54. Teranishi, T. & Sakamoto, M. Charge separation in type-II semiconductor heterodimers. *J. Phys. Chem. Lett.* **4**, 2867–2873 (2013).

55. Xu, Q. et al. Direct Z-scheme photocatalysts: Principles, synthesis, and applications. *Mater. Today* **21**, 1042–1063 (2018).

56. Zhang, G. et al. A mini-review on ZnIn$_2$S$_4$-Based photocatalysts for energy and environmental application. *Green Energy Environ* **7**, 176–204 (2020).

57. Chen, S., Hu, Y., Meng, S. & Fu, X. Study on the separation mechanisms of photogenerated electrons and holes for composite photocatalysts g-C$_3$N$_4$-WO$_3$. *Appl. Catal. B* **150**, 564–573 (2014).

58. Zhao, W. et al. Fabrication of a novel p–n heterojunction photocatalyst n-BiVO$_4$@p-MoS$_2$ with core–shell structure and its excellent visible-light photocatalytic reduction and oxidation activities. *Appl. Catal. B* **185**, 242–252 (2016).

59. Yuan, G. et al. Research progress on photocatalytic reduction of Cr (VI) in polluted water. *Bull. Chem. Soc. Jpn.* **94**, 1142–1155 (2021).

60. Wang, J. et al. Visible-light-driven double-shell SnIn$_4$S$_8$/TiO$_2$ heterostructure with enhanced photocatalytic activity for MO removal and Cr (VI) cleanup. *Appl. Surf. Sci.* **587**, 152867 (2022).

61. Mehrizad, A. & Gharbani, P. Application of central composite design and artificial neural network in modeling of reactive blue 21 dye removal by photo-ozonation process. *Water Sci. Technol* **74**, 184–193 (2016).

62. Xu, P. et al. Surfactant-assisted hydrothermal synthesis of rGO/SnIn$_4$S$_8$ nanosheets and their application in complete removal of Cr (vi). *RSC Adv* **8**, 5749–5759 (2018).

63. Ai, L. et al. Controlled growth of single-crystalline Bi. 333 (Bi$_6$S$_9$) Br nanorods under hydrothermal conditions for enhanced photocatalytic reduction of Cr (VI). *J. Alloys Compd.* **842**, 155879 (2020).

64. Yao, L., Chen, Z., Li, J. & Shi, C. Creation of oxygen vacancies to activate lanthanum-doped bismuth titanate nanosheets for efficient synchronous photocatalytic removal of Cr (VI) and methyl orange. *J. Mol. Liq.* **314**, 113613 (2020).

65. Sun, M. et al. Fabrication of MOF-derived tubular In$_2$O$_3$@ SnIn$_4$S$_8$ hybrid: Heterojunction formation and promoted photocatalytic reduction of Cr (VI) under visible light. *J. Colloid Interface Sci* **596**, 278–287 (2021).

66. Nguyen, V. H. et al. Composite photocatalysts containing MIL-53 (Fe) as a heterogeneous photo-Fenton catalyst for the decolorization of rhodamine B under visible light irradiation. *J. Environ. Chem. Eng.* **6**, 7434–7441 (2018).

67. Xu, S., Liu, Z., Zhang, M. & Guo, L. Piezotronics enhanced photocatalytic activities of Ag-BaTiO$_3$ plasmonic photocatalysts. *J. Alloys Compd.* **801**, 483–488 (2019).

68. Xu, P. et al. Z-Schemed WO$_3$/rGO/SnIn$_4$S$_8$ sandwich nanohybrids for efficient visible light photocatalytic water purification. *Catalysts* **9**, 187 (2019).

69. Spilarewicz-Stanek, K., Jakimińska, A., Kisielewska, A., Batory, D. & Piwoński, I. Understanding the Role of Silver Nanostructures and Graphene Oxide Applied as Surface Modification of TiO$_2$ in Photocatalytic Transformations of Rhodamine B under UV and Vis Irradiation. *Materials* **13**, 4653 (2020).

ACKNOWLEDGEMENTS

AUTHOR CONTRIBUTIONS

S.A.: Investigation, Original draft preparation; A.M.: Supervision, Software, Formal analysis, Reviewing and Editing; M.A.B.: Project administration, Supervision; M.E.R.: Visualization, Reviewing and Editing; P.G.: Data Curation, Validation.

COMPETING INTERESTS

The authors declare no competing interests.

ADDITIONAL INFORMATION

Supplementary information The online version contains supplementary material available at https://doi.org/10.1038/s41545-023-00246-w.

Correspondence and requests for materials should be addressed to Ali Mehrizad.

Reprints and permission information is available at http://www.nature.com/reprints

Publisher's note Springer Nature remains neutral with regard to jurisdictional claims in published maps and institutional affiliations.